N87-29445

RECONSTRUCTION OF A THREE-DIMENSIONAL, TRANSONIC ROTOR FLOW
FIELD FROM HOLOGRAPHIC INTERFEROGRAM DATA

John K. Kittleson* and Yung H. Yu*
Aeromechanics Laboratory, U.S. Army Research and Technology Laboratories — AVSCOM
NASA Ames Research Center, Moffett Field, California

Abstract

Holographic interferometry and computer-assisted tomography (CAT) are used to determine the transonic velocity field of a model rotor blade in hover. A pulsed ruby laser recorded 40 interferograms with a 2-ft-diam view field near the model rotor-blade tip operating at a tip Mach number of 0.90. After digitizing the interferograms and extracting fringe-order functions, the data are transferred to a CAT code. The CAT code then calculates the perturbation velocity in several planes above the blade surface. The values from the holography-CAT method compare favorably with previously obtained numerical computations in most locations near the blade tip. The results demonstrate the technique's potential for three-dimensional transonic rotor flow studies.

Nomenclature

a_0 = speed of sound, ft/sec

A = wave amplitude

C = blade chord, ft

$f(x')$ = filter function

I = irradiance

k = Gladstone-Dale constant, $ft^3/slug$

L = path length, ft

n = refractive index

n_0 = ambient refractive index

N = fringe-order number

R = spanwise coordinate, ft

R_0 = blade span, ft

t = hologram amplitude transmittance

U_c = reconstruction wave complex amplitude

U_i = transmitted wave complex amplitude

U_r = reference wave complex amplitude

U_{01} = ambient object wave complex amplitude

U_{02} = test object wave complex amplitude

V = perturbation velocity, ft/sec

---

*Research Engineer. Member AIAA.

This paper is declared a work of the U.S. Government and therefore is in the public domain.

x' = projection coordinate, ft

X = chordwise coordinate, ft

Y = height above blade centerline, ft

β = film proportionality constant

γ = ratio of specific heats

$\Delta\phi$ = optical path-length difference (OPD)

θ = field projection angle, deg

λ = laser wavelength, ft

ρ = air density, $slug/ft^2$

ρ_0 = ambient air density, $slugs/ft^3$

Ω = blade rotational speed, rpm

Introduction

On many helicopters, the rotor blade's advancing tip encounters transonic flow during forward flight. At these high Mach numbers, the rotor blade's performance suffers from compressibility effects that often cause shock waves to form near the blade tip; the shocks can extend to the acoustic far-field. Through theoretical and computational investigations, researchers attempt to understand the local shock generation of high-tip-speed rotors and its propagation to the far-field. However, because of the problem's complexity and the difficulty of obtaining detailed experimental information about the flow, accurate means for confirming transonic rotor-blade designs have been notably lacking.

Shock waves cause a number of aerodynamic, dynamic, and acoustic problems on high-speed helicopter rotor blades. First, the shock rapidly increases the aerodynamic drag through energy dissipation, flow separation, and wave effects. Second, local shocks cause sudden large changes in pitching moment which can excite various blade torsional modes. As the blade rotates in forward flight, its Mach number and angle of attack vary. The shock appears on the advancing side of the rotor disk and often results in large chordwise movements; these movements can be in opposite directions on the upper and lower surfaces as the Mach number and angle of attack change during each revolution. The changing shock positions on the upper and lower surfaces cause an unsteady loading, which produces fluctuating pitching moments. These moments can cause unexpected blade motions, oscillating loads on pitch links, and vibrations throughout the entire aircraft. Third, shock waves on an advancing-blade surface can "delocalize" (Ref. 1) and extend directly to the far-field. Large amounts of acoustic energy radiate in front of the helicopter near the tip-path plane. This helicopter impulsive noise is

annoying in general and too easily detected in military applications.

In an attempt to describe the transonic rotor flow field and to resolve the problems associated with it, promising theoretical models[2] and numerical codes[3,4] have been developed. The numerical codes compare favorably with blade-pressure measurements,[5] but are not yet verified at points away from the blade's surface.

Previous attempts to measure the flow field have been severely limited. Pressure-instrumented airfoils are expensive and difficult to fabricate—especially in scale models. In addition, pressures can be measured only at the blade surface. Hot-wire anemometry requires that a probe be positioned within the field, therefore disturbing the flow. Laser velocimetry requires flow-seeding and, when shock waves are present, it is uncertain whether the seeds follow the flow faithfully. Both hot-wire anemometry and laser velocimetry can take only point-by-point measurements, requiring large amounts of running time to survey the rotor's three-dimensional field, a distinct disadvantage for rotor testing. Schlieren and shadowgraph photography provide only a qualitative two-dimensional representation of a three-dimensional flow. And Mach-Zehnder interferometry provides quantitative information, but is extremely difficult to use in a large-scale experiment. Clearly, another experimental technique which overcomes these limitations must be employed.

Holographic interferometry is an effective diagnostic technique for making transonic flow measurements.[6] Previous investigations[7,8] in which two-dimensional flows over airfoils were studied show that accurate quantitative information is obtainable using holographic interferometry. However, the transonic flow around a helicopter rotor blade is three-dimensional and requires a tomographic technique to compute the correct flow information from several interferograms. To date, most applications of this technique have been limited to axisymmetric flow or to simple three-dimensional flow with a small model under ideal laboratory conditions.[9,10]

This paper discusses the procedures necessary to obtain quantitative measurements of a transonic, three-dimensional flow field near a rotor-blade tip, using holographic interferometric data and CAT. Though most helicopter rotor problems caused by shock waves occur during forward flight, this experiment investigates the steady problem (hover), which simulates many physical phenomena of forward flight.[11] The method for recording interferograms and example interferograms is included, and the steps that must be followed in extracting quantitative information from the interferograms are outlined. The technique's potential for measuring three-dimensional transonic rotor flows is demonstrated, and the results it yields are compared with those from previously performed numerical computations.

Background Concepts

For the experiment to be successful, it is necessary to 1) record high-quality interferograms near a rotor-blade tip from multiple viewing angles, and 2) implement a suitable CAT code with the interferogram data. Familiarity with holography,

holographic interferometry, and computer-assisted tomography principles provides the necessary insight for understanding this technique.

Holography

Holography is a two-step imaging process in which diffracted light waves are recorded and reconstructed.[12,13] The first step is recording, or storing, the hologram. This is accomplished by dividing a single coherent laser beam into two beams and exposing a photographic film to the two light waves, as shown in Fig. 1a. The object wave, which is the wave containing the flow information, passes through the measured field (the air near the blade tip in this experiment). The second wave, the reference wave, passes around the field. By adding the coherent reference wave to the object wave, the photographic film records a high-frequency interference pattern. Once the film is developed, it is known as a hologram, which is a complicated diffraction grating.

The second step in holography is reconstruction, or playing back the hologram. This is accomplished in two ways. First, a reconstruction wave identical to the reference wave illuminates the hologram (Fig. 1b). The hologram diffracts the reconstruction wave and produces a replica of the original object wave, forming the original object's virtual image. In the second method of reconstruction, a reconstruction wave conjugate to the reference wave illuminates the hologram (Fig. 1c). The hologram diffracts the conjugate wave forming the original object's real image. The real image may be photographed without the use of a lens by placing a sheet of photographic film in the real image space.

Several important characteristics of holography are applicable to the experiment at hand. There are very few geometrical constraints in a holographic optical system; thus, holography can be applied in a large-scale, nonlaboratory environment. Note that recording and reconstruction of the hologram can be done in different locations if the reference wave is reproducible. This allows the reconstruction to be done in a laboratory, far from the harsh environment in which the hologram was previously recorded. The reference wave serves only as a method of recording and reconstructing the object wave. Thus, a hologram does not produce quantitative information about the field of interest. To obtain quantitative information (in the form of interference fringes) an interferogram must be recorded.

Holographic Interferometry

Holographic interferometry is the interferometric comparison of two object waves recorded holographically (see the Appendix for further detail). In this experiment, the two object waves are recorded sequentially in time with double-exposure holographic interferometry. The interferogram is recorded by first exposing a photographic film to a reference wave and an "undisturbed" object wave. Later in time, the same photographic film is exposed to a reference wave and to a second "disturbed" object wave.

When the holographic interferogram is reconstructed, the virtual or real image shows the object (the transparent field) with an

interference fringe pattern. The fringe pattern represents the difference between the "undisturbed" and "disturbed" flow states. The irradiance of the reconstructed wave is proportional to

$$I = |U_{01} + U_{02}|^2$$

which can be written as[12,13]

$$I = 2A^2[1 + \cos(\Delta\phi)] \tag{1}$$

Equation (1) represents the interferogram with a fringe pattern of dark and bright fringes of constant optical path-length difference (OPD) $\Delta\phi$, where $\Delta\phi$ is given by

$$\Delta\phi = \int [n(x,y,z) - n_0]ds = N\lambda \tag{2}$$

To determine the flow-field properties, the line integral of Eq. (2) must be inverted and solved for $n(x,y,z)$, the refractive index at a specific point in the field.

In a two-dimensional flow (i.e., the flow over a fixed airfoil in a wind tunnel), the evaluation of Eq. (2) is simplified. Since the refractive index is constant across the width of the test section L, Eq. (2) becomes

$$n(x,y) = n_0 + N\lambda/L \tag{3}$$

In a two-dimensional flow, the fringes on an interferogram are contours of constant refractive index and the refractive index at any point in the field can be determined from a single interferogram. However, since the transonic flow near a rotor-blade tip is three-dimensional, Eq. (3) cannot be used. To invert Eq. (2) and solve for the refractive index at a specific point in the field, computer-assisted tomography (CAT) must be employed.

Computer-Assisted Tomography

Tomography is a mathematical technique for reconstructing a three-dimensional field from its two-dimensional projections (see Refs. 14 and 15 for a wide variety of applications). A projection of a three-dimensional field is the fringe pattern recorded on an interferogram. All methods require multidirectional projection data of the field. Tomographic codes develop in two directions: 1) iterative algebraic reconstruction techniques,[16] and 2) Fourier transform techniques. A version of the latter method, termed filtered back-projection,[17,18] appears most suitable for this application.

Most Fourier transform techniques employ back-projection. Projection data from the field are recorded in one plane at several azimuthal angles around the field. For example, one projection of a uniform absorbing disk is shown in Fig. 2a (taken from Ref. 19). Beyond the disk boundary (no path length through the disk), the light ray's OPD is unchanged, producing no interference fringes. Near the disk boundary (short path length through the disk), the light ray's OPD is changed slightly, producing a few interference fringes. And near the disk center (long path length through the absorbing disk), the light ray's OPD is changed substantially, producing several interference fringes. Similar projections

(fringe number vs position) at different azimuthal angles are also recorded. Each projection is then back-projected, or smeared back along the direction in which it was recorded (Fig. 2b). Values are added point by point to form a reconstruction of the field. Unfortunately, simple back-projection produces an undesirable spoke pattern which severely degrades the quality of the reconstructed field.

To eliminate the spoke pattern, the back-projections are filtered. A one-dimensional convolution (indicated by an asterisk) is performed between each projection and an appropriate filter function (see Ref. 20 for a discussion of filter functions) before back-projection, as shown in Fig. 3a (taken from Ref. 19). Each filtered projection is then back-projected over the reconstruction space (see Fig. 3b). The negative sidelobes introduced by the filter eliminate the spoke pattern during the point-by-point addition process. With many projections, this technique yields an accurate reconstruction of the original field.

Procedure

Several steps must be performed to quantitatively reconstruct the three-dimensional transonic field near a model helicopter blade tip. First, several holographic interferograms must be recorded along planes perpendicular to the rotor tip-path plane at various azimuthal angles (Fig. 4). Data must then be extracted from the interferograms. This can be done 1) manually, 2) by using a graphic tracing tablet,[21] or 3) by using a system that digitizes the interferograms and extracts fringe-order numbers. The digital interferogram evaluation technique was used; it will be presented in detail by Becker and Yu (Ref. 22). Finally, the data are transferred as input to a tomography code, which computes the refractive index at specific points in a horizontal plane above the blade surface. This procedure is repeated in several planes to yield a reconstruction of the entire three-dimensional field.

Recording Holographic Interferograms

The holographic system for recording interferograms near a model rotor blade was assembled in the Aeromechanics Laboratory Anechoic Hover Chamber. Figure 5 shows a schematic of the optical system and Fig. 6 shows the Anechoic Hover Chamber. A ruby laser with a 20-nsec pulse width, a 694.3-nm wavelength, and a power of 1 J "freezes" the rotating blade at any desired azimuthal angle. A beam-splitter divides the laser beam into two separate beams at the laser outlet. A microscope objective lens expands the object beam to fill a 24-in.-diam spherical mirror. Since the foci of both the objective lens and the spherical mirror coincide, a collimated plane wave forms as the beam passes through the rotor area. The object beam then strikes a second 24-in.-diam spherical mirror, emerges as a converging wave, and illuminates a 4-in. by 5-in. photographic plate. The reference beam is lengthened by causing it to strike several plane mirrors. This beam must be lengthened so that the difference in the path lengths of the object and reference beams is less than the coherence length of the laser (one of the very few, and

easily met, geometrical constraints in a holographic system). The reference beam is expanded by an objective lens, then collimated with a 5-in.-diam lens; finally, it is directed toward the film so that it overlaps the object beam.

The entire procedure is conducted from outside the hover chamber, once the optical system is aligned. Firing the laser, changing the photographic film plates, and controlling the test conditions are all done by remote control. Recall that to record an interferogram, two exposures at different times (different flow states) must be made on a single film plate. The film records the first exposure while the rotor blade remains stationary. In this case, the air has no velocity and therefore has a uniform refractive-index distribution. The film records the second exposure while the blade rotates at the desired speed. The nonhomogeneous refractive-index distribution in this case introduces phase changes in the second object wave, producing interference fringes on the film plate. This double-exposure recording procedure repeats at various angles around the flow by synchronizing the laser pulse with the desired blade position. Because of the long optical pathlengths (90 ft), the recording system is very sensitive to vibrations of the optical components. At several azimuthal angles, it was necessary to record multiple interferograms to obtain one high-quality interferogram. The photographic plates are then removed from the recording system in the hover chamber, developed, and reconstructed in a laboratory for further processing.

Holographic interferograms record the flow near a hovering 1/7-scale (geometric) model UH-1H rotor with untwisted NACA 0012 airfoil sections. The blade runs at a tip Mach number of 0.90 so that the flow is transonic and a shock wave is present.[1] This model normally uses two blades; however, in views along the span, the optical beam would pass through the refractive-index field of both blades. Because the refractive-index fields of the two blades are inseparable at these angles, a single-bladed rotor with a counterbalance is used instead (Fig. 7).

Holographic interferograms near a transonic rotor blade are recorded at 40 different viewing angles. The blade rotates in a clockwise direction and can be captured at any desired viewing angle with the pulsed laser. The tomography code requires flow data from certain viewing angles within a 180° range. Numerical simulation results[2,3] using numerical computations of the flow[3] suggest recording interferograms from $\theta = 8°$ to $\theta = 40°$ and from $\theta = 140°$ to $\theta = 186°$ in 2° increments, as defined in Fig. 8. The missing views, $\theta = 42°$ to $\theta = 138°$, were presumed to have very few interference fringes and were not utilized.

Illustrated in Fig. 8 are examples of holographic interferograms recorded near the model blade tip. The fringe pattern's appearance depends on the viewing direction. Interferograms recorded along the chord (near $\theta = 90°$) display very few interference fringes, since the optical rays pass through the field's thinnest (weakest) region. No observable details are present in these views. However, in views along the span , (near $\theta = 0°$ or $\theta = 180°$), numerous fringes are visible, because the optical rays pass through the

longest (strongest) region within the field. The leading-edge stagnation point, shock structures, boundary-layer separation, and wake system are clearly visible. In particular, a lambda shock ($\theta = 180°$) and the radiated shock ($\theta = 186°$) appear above the blade. Several interferograms are described in detail in Ref. 24.

Data Extraction

There is an important step that must be taken between recording the interferograms and making the tomographic reconstruction: evaluating the interferograms. During this evaluation, integrated quantitative information is extracted from the interferogram fringe pattern. Previously, most interferograms were evaluated manually, which is a time-consuming and inaccurate procedure. To overcome these limitations, a scheme for digital interferogram evaluation was implemented that digitizes, enhances, and records fringe coordinates and numbers from the interferograms (see Ref. 22 for a discussion of this system).

An image-processing system (De Anza IP-6400) connected to a VAX 11/780 host computer digitizes the 40 interferograms. A one-dimensional fringe evaluation is then performed by assigning fringe-order numbers to each interferogram. To make a correct assignation of fringe-order numbers, some information about the flow is required. Positive values are assigned to high-density regions and negative values to low-density regions. The zero fringe-order number is assigned to the regions where the field is undisturbed. Each interferogram is then scanned at a desired height above the blade, as shown in Fig. 9a. For each projection angle, fringe numbers and locations are recorded (Fig. 9b) and stored. The fringe-order functions serve as input data for the CAT code to reconstruct the field in one horizontal plane above the blade surface.

CAT Reconstruction

Fringe-order functions are transferred to the filtered back-projection CAT code which computes the refractive-index field at specific points in a chosen horizontal plane above the blade surface. The code assumes refractionless light rays; therefore, each horizontal plane can be treated independently, even though data for each plane is taken from one set of interferograms. The perturbation velocity is computed by first converting refractive index to density, using the Gladston-Dale relation:

$$\rho = (n - 1)/k$$

Density is then converted to perturbation velocity from a form of Bernoulli's equation for steady (with respect to the rotation blade), compressible, isentropic flow:

$$V = -\Omega R + \left\{ (\Omega R)^2 - \frac{2a_0^2}{\gamma - 1} \left[\left(\frac{\rho}{\rho_0} \right)^{\gamma-1} - 1 \right] \right\}^{1/2} \quad (4)$$

The procedure is repeated in several planes above the blade to reconstruct the entire three-dimensional field near the model blade tip.

152

Reconstruction Results

The holography-CAT reconstruction of the blade-tip velocity field is compared with numerical computations. The computations used here are conservative, mixed-difference solutions of the transonic small-disturbance equation. Results from both sources are presented in four horizontal planes, as identified in Fig. 10a. Three plot types are used to visualize the flow field. First, velocity contours are given in plan view (see Fig. 10b), where the blade's leading and trailing edges are at X/C = 0.0 and X/C = 1.0, respectively. The blade tip is located at R/R_0 = 1.0, the rotation center is at R/R_0 = 0.0, and the blade rotates in a clockwise direction. Second, perspective views are displayed in which velocity values are plotted along the vertical axis. The data and geometry are identical to the contour plots, though the data are viewed from near the rotor hub. Third, velocity distributions are shown at six radial locations (see Fig. 10b) for each plane.

Figure 11 compares the velocity contours derived from the holographic-CAT method and the numerical computations near the blade surface (Y/C = 0.08). Both methods display low-velocity regions near the leading and trailing edges, and also display a high-velocity region over the blade surface containing a shock at approximately X/C = 0.60 near the blade tip. The general contour shapes show a strong resemblance except near the blade tip (roughly the last 5% of blade span). The maximum velocity region appears at the shock foot in the computational analysis, but it appears closer to the leading edge and farther from the shock foot in the holography-CAT results.

Figure 12 shows velocity values for the same plane in perspective view. Again, the general flow shapes appear very similar. The major difference between the two results is the roughness (minor "ridges") in the reconstructed flow. This may be due to reconstruction artifacts caused by noncontinuous data (interferograms recorded in 2° azimuthal increments) or by noise (erroneous fringes) in the interferogram data caused by optical component motion. Figure 13 compares velocity distributions at six radial locations. The roughness of the reconstructed flow can be seen throughout the figures. Also, the holography-CAT method determines the shock location to be slightly more downstream (3%) than does the numerical code solution. The major differences can be observed in Fig. 13d, where the discrepancies at the leading edge and over the blade surface are clearly visible. The leading edge (X/C = 0.0) difference may result from a breakdown of the small crossflow assumption [Eq. (4)] near the blade tip. The difference over the blade surface (X/C = 0.2 to X/C = 0.6) may be attributed to the existence of a lambda shock, in the interferogram data (i.e., Fig. 9a), which cannot be predicted by the nonviscous numerical potential code. A lambda shock was also observed in Schlieren photographs from a previous wind-tunnel test (Fig. 14, taken from Ref. 25) using the same airfoil and tip Mach number.

Figure 15 compares the velocity contours from both the holography-CAT method and numerical code at Y/C = 0.22 (near the upper region of the lambda shock). The general velocity contours show an excellent agreement in both shape and magnitude

throughout the plane. The maximum velocity region on the blade surface (near X/C = 0.50, R/R_0 = 0.96) match much closer in this plane than in the plane near the blade surface (Fig. 11). The perspective view of Fig. 16 also shows an excellent agreement in shape and magnitude. Again, the most noticeable difference is the extra ridges in the reconstructed flow at the same locations and orientations as seen in the previous plane (Fig. 12a). The velocity distributions in this plane (Fig. 17) compare favorably, especially inboard of the blade tip (see Figs. 17a-17c), as well as at the blade tip (Fig. 17d). The lambda shock's effect near the tip is apparently weaker in this plane; thus, the velocity distribution magnitudes and shapes are much closer than those in Fig. 13.

Figure 18 compares velocity contours at Y/C = 0.49 above the blade. The velocity contour shapes and magnitudes are similar in all regions except that the holography-CAT method shows the maximum velocity point to be slightly (1% span) outboard of the numerical result. The extra ridges seen in the perspective view (Fig. 19) are in approximately the same location and orientation as those in the previous plane; however, the magnitude of the ridges has decreased. Figure 20 shows velocity distributions for this plane. There is good agreement at all locations except beyond the blade tip (Fig. 20e) where the holography-CAT method shows slightly larger velocity magnitudes.

Finally, Fig. 21 shows velocity contours for Y/C = 1.17. The velocity contours match throughout, though there are no distinguishing features in the flow at this height above the blade surface. In this plane, the extra ridges are almost unobservable in the perspective view (Fig. 22). The velocity distributions of Fig. 23 also show a strong similarity between the two methods at all radial locations, for both results show that this plane is at the perturbed flow's upper extent.

Overall, the agreement between the holography-CAT results and the numerical solution is extremely encouraging. However, comparisons with other experimental data sources are required before a final decision can be made about the holography-CAT results. Several discrepancies must be resolved. First, data from pressure-instrumented blades will aid in confirming the shock location and whether a lambda shock does exist in the flow. Second, the extra ridges appearing in the reconstructed results must be eliminated or reduced; the ridges may be caused by poor data recorded in the interferograms. To improve the quality of the interferograms, a modified optical system (for both hover and forward flight testing) is necessary. In addition, neither the holography-CAT reconstruction nor the numerical code solutions compute the expected shock strength beyond the blade tip. Acoustic measurements indicate a much stronger radiated shock than is indicated by these two results.

Concluding Remarks

The holographic interferometry computer-assisted tomography technique proved to be a highly effective way of measuring the three-dimensional, transonic flow field near a model

153

rotor-blade tip. Results from this method compare favorably with those of numerical computations, except very near the tip region. That discrepancy may be due to the existence of a lambda shock recorded by the interferograms (and in previous Schlieren photographs) which is not predicted by the nonviscous potential code. In other regions, the velocity distributions along the chord are similar in both shape and magnitude. However, the results from the technique must be further verified against other experimental data.

Since this is the first successful implementation of the holographic interferometry, computer-assisted tomography method in rotor flow studies, many improvements are indicated. For example, the optical system must be improved so that better quality interferograms can be recorded, and an automatic fringe-reading technique must be completed so that the time required to evaluate interferograms can be shortened. Upon verification of these results and after the system is improved, measurements of other model rotor-blade flow fields, including those of forward flight, will be performed.

Appendix: Holographic Interferometry

Double-exposure holographic interferometry is the interferometric comparison of two object waves that are recorded holographically sequentially in time. The interferogram is recorded by first exposing a photographic film to a reference wave and an "undisturbed" object wave, as shown in Fig. 24a. Later in time, the same photographic plate is exposed to a reference beam and a second "disturbed" object wave, as shown in Fig. 24b. The irradiance at the film plane is

$$I = |U_r + U_{01}| + |U_r + U_{02}|$$

$$= 2I_r + I_{01} + I_{02} + U_r^*(U_{01} + U_{02}) + U_r(U_{01} + U_{02})^*$$

(A1)

The last two terms of Eq. (A1) represent the interference pattern recorded on the film, which contains both amplitude and phase information about the two reference and the two object waves. The amplitude transmittance of the developed film, called a holographic interferogram, is

$$t = (2I_r + I_{01} + I_{02}) + U_r^*(U_{01} + U_{02})$$

$$+ U_r(U_{01} + U_{02})^*$$

When the reconstruction wave illuminates the interferogram, as shown in Fig. 24c, the transmitted light is

$$U_i = U_c t$$

$$= U_c(2I_r + I_{01} + I_{02}) + U_r^* U_c(U_{01} + U_{02})$$

$$+ U_r U_c(U_{01} + U_{02})^*$$

(A2)

The second term in Eq. (A2) is the "composite" virtual image reconstruction of the two object waves $(U_{01} + U_{02})$. By illuminating the interferogram with a conjugate reconstruction wave

(Fig. 24d), the transmitted light is

$$U_i = U_c^* t$$

$$= U_c^*(2I_r + I_{01} + I_{02}) + U_r^* U_c^*(U_{01} + U_{02})$$

$$+ U_r U_c^*(U_{01} + U_{02})^*$$

(A3)

The third term in Eq. (A3) is the composite real image reconstruction of the two object waves $(U_{01} + U_{02})$, which is the image that is photographed and presented in this paper.

The primary reason for using holographic interferometry is that it possesses a property called cancellation of path-length errors. In a holographic interferometer, the interfering waves divide temporally. That is, the two interfering (object) waves are recorded at two different times but travel the same path through the optical system (recall that the reference wave serves only to store and play back the interferogram). Since there is no difference between the two path lengths of the interfering object waves in the optical system, only changes in the path lengths caused by the different states of the test field are displayed as fringes in the interferogram. This leaves a useful interferogram, even though low-quality optics are used. Therefore, holographic interferometry can be used in a large-scale experiment in which relatively low-quality optics are used and still yield high-quality interferograms.

References

[1]Schmitz, F. H. and Yu, Y. H., "Transonic Rotor Noise—Theoretical and Experimental Comparisons," Vertica, Vol. 5, 1981, pp. 55-74.

[2]Isom, M. P., "Unsteady Subsonic and Transonic Potential Flow Over Helicopter Rotor Blades," NASA CR-2463, 1974.

[3]Caradonna, F. X., "The Transonic Flow on a Helicopter Rotor," Ph.D. dissertation, Stanford U., Stanford, Calif., Mar. 1978.

[4]Arieli, R. and Tauber, M., "Computation of Subsonic and Transonic Flow about Lifting Rotor Blades," AIAA Paper 79-1667, 1979.

[5]Tung, C., Caradonna, F. X., and Boxwell, D. A., "The Prediction of Transonic Flows on Advancing Rotors," Proceedings of the 40th Annual National Forum of the American Helicopter Society, Arlington, Va., May 1984.

[6]Trolinger, J. D., "Laser Instrumentation for Flow Field Diagnostics," AGARDograph 186, 1974.

[7]Johnson, D. A. and Bachalo, W. D., "Transonic Flow About a Two-Dimensional Airfoil—Inviscid and Turbulent Flow Properties," AIAA Paper 78-1117, 1978.

[8]Bachalo, W. D., "Measurements of Supercritical Airfoil Flow Fields Using Interferometry," Douglas Aircraft Company, McDonnell Douglas Corporation, Mar. 1982.

[9]Matulka, R. D. and Collins, D. J., "Determination of Three-Dimensional Density Fields from Holographic Interferometry," Journal of Applied Physics, Vol. 42, 1971, pp. 1109-1119.

[10]Sweeney, D. W. and Vest, C. M., "Reconstruction of Three-Dimensional Refractive Index Fields from Multidirectional Interferometric Data," Applied Optics, Vol. 12, 1973, pp. 2649-2664.

[11]Boxwell, D. A., Yu, Y. H., and Schmitz, F. H., "Hovering Impulsive Noise: Some Measured and Calculated Results," Vertica, Vol. 3, 1979, pp. 35-45.

[12]Vest, C. M., Holographic Interferometry, Wiley-Interscience, 1979.

[13]Collier, R. J., Burckhardt, C. B., and Lin, L. H., Optical Holography, Academic Press, 1971.

[14]Marr, E. B., ed., Proceedings of the International Workshop on Techniques of Three-Dimensional Reconstruction, BNL 20425, Brookhaven National Laboratory, Upton, N.Y., 1976.

[15]Technical Digest of the 1975 Optical Society of American Technical Meeting, Stanford University, OSA, Washington, D.C., 1975.

[16]Gordon, R. and Herman, G. T., International Review of Cytology, Vol. 38, 1974.

[17]Shepp, L. A. and Logan, B. F., "The Fourier Reconstruction of a Head Section," IEEE Transactions on Nuclear Science, Vol. NS-21, 1974, pp. 21-42.

[18]Ramachandran, G. N. and Lakshminarayanan, A. V., "Three-Dimensional Reconstruction from Radiographic and Electron Micrographic Applications of Convolutions Instead of Fourier Transforms," Proceedings of the National Academy of Sciences of the United States of America, Vol. 68, 1971, pp. 2236-2240.

[19]Swindell, W. and Barrett, H. H., "Computerized Tomography: Taking Sectional X-rays," Physics Today, Dec. 1977, pp. 32-41.

[20]Herman, G. T., "Image Reconstruction from Projections, Implementation and Applications," Topics in Applied Physics, Vol. 32, Springer, Berlin, 1979.

[21]Modarress, D., Tan, H., and Trolinger, J., "Tomographic Reconstruction of Three-Dimensional Flow over Airfoils," Paper No. 85-0479 to be presented at AIAA 23rd Aerospace Sciences Conference, Reno, Nev., Jan. 14-17, 1985.

[22]Becker, F. and Yu, Y. H., "Application of Digital Interferogram Evaluation Technique to the Measurement of Three-Dimensional Flow Fields," Paper No. 85-0037 to be presented at AIAA 23rd Aerospace Sciences Conference, Reno, Nev., Jan. 14-17, 1985.

[23]Snyder, R. and Hesselink, L., "Optical Tomography for Flow Visualization of the Density Field Around a Revolving Helicopter Rotor Blade," Applied Optics, Vol. 23, 1984, pp. 3650-3656.

[24]Kittleson, J. K., "A Holographic Interferometry Technique for Measuring Transonic Flow near a Rotor Blade," Proceedings of the Ninth European Rotorcraft Forum, B, Stresa, Italy, Sept. 1983.

[25]Schmitz, F. H., Boxwell, D. A., and Vause, C. R., "High-Speed Helicopter Impulsive Noise," Journal of the American Helicopter Society, Oct. 1977.
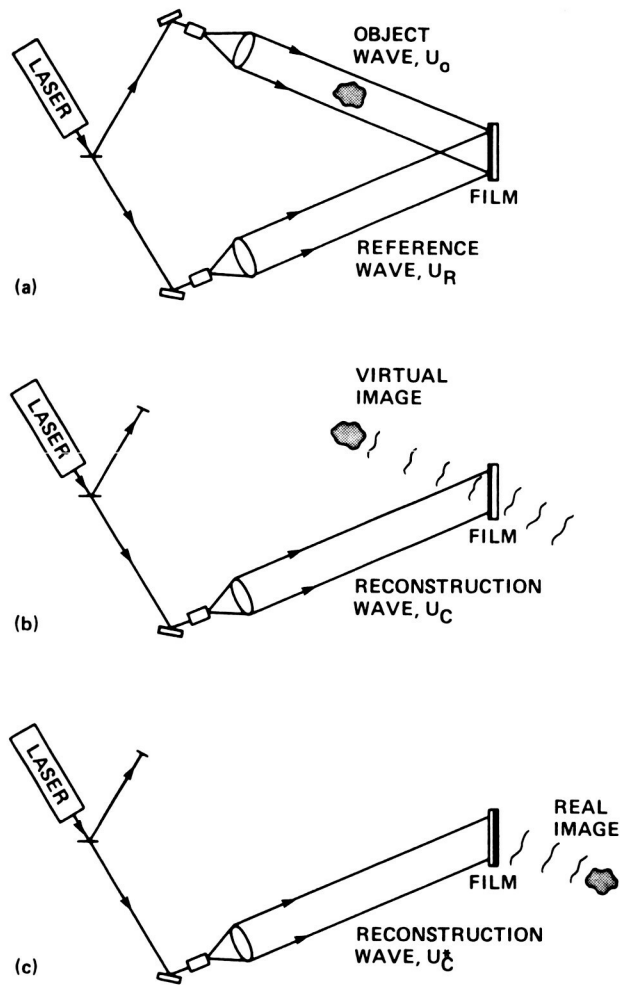
Fig. 1 Optical holography recording and reconstruction. a) Recording the hologram; b) reconstruction of the true, virtual image; c) reconstruction of the conjugate, real image.
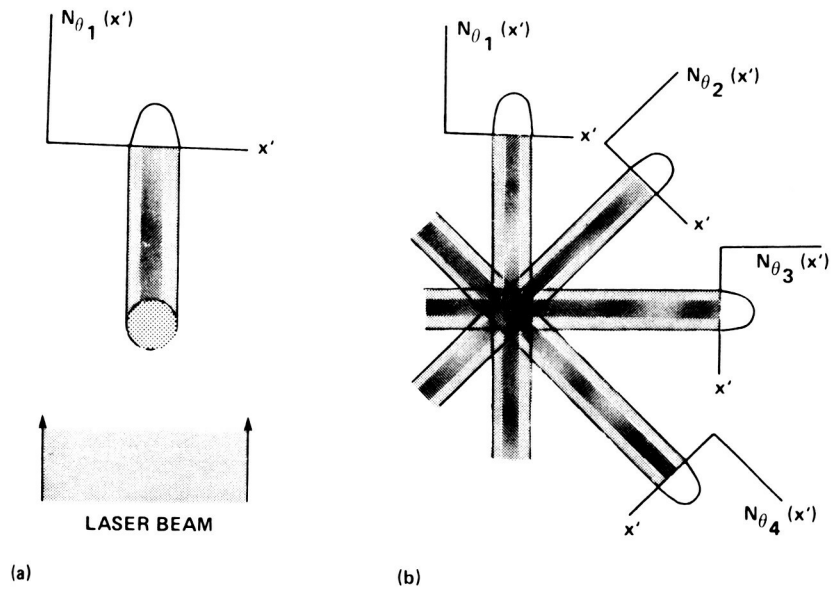

Fig. 2 Back-projection. a) One projection of an absorbing disk; b) back-projecting consists of smearing each projection back along the direction in which the original projection was made. (From Ref. 19.)
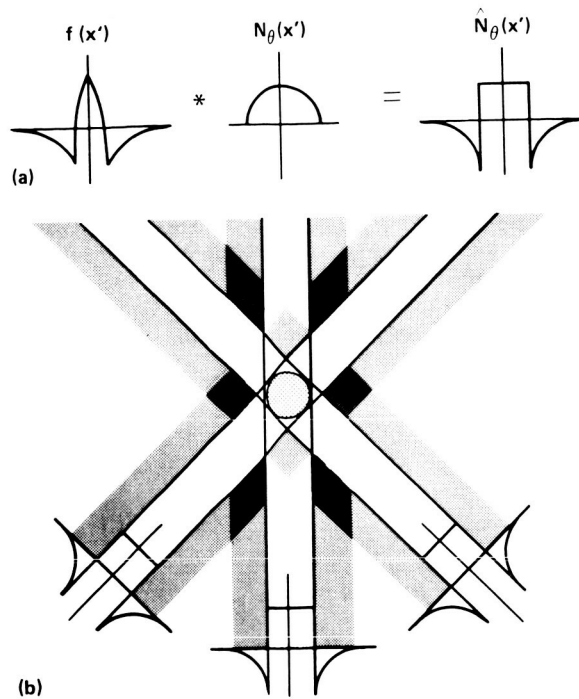
$f(x')$ $N_\theta(x')$ $\hat{N}_\theta(x')$

(a)

*

=

(b)

Fig. 3 Filtered back projection. a) The projection data are convolved (filtered) with a suitable process-ing function before back-projection; b) three back-projections of an absorbing disk. (From Ref. 19).

FILM

BLADE

FILM

TRANSPARENT
FIELD OF INTEREST

FILM

$$\Delta\phi = \int (n - n_o)\,ds = N\lambda$$
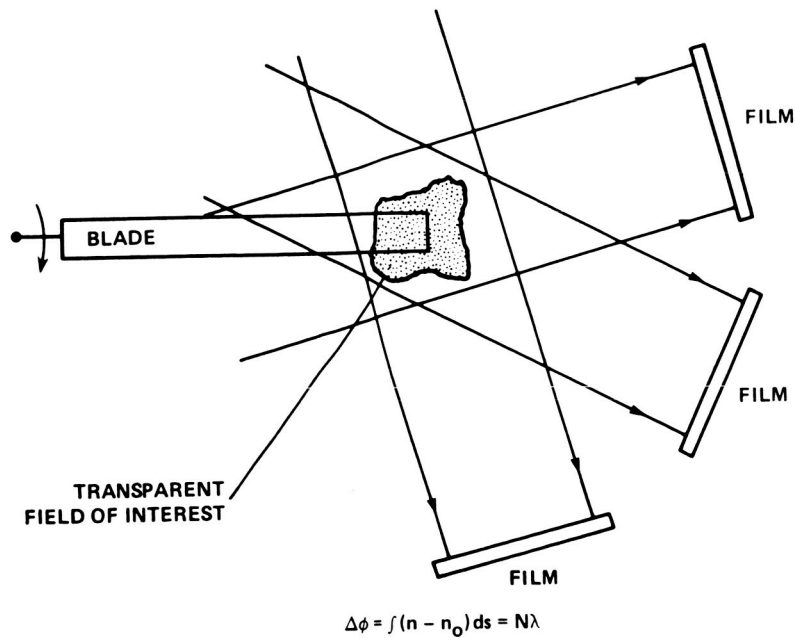
Fig. 4 Recording interferograms at various angles around the field of interest for tomographic reconstruction.
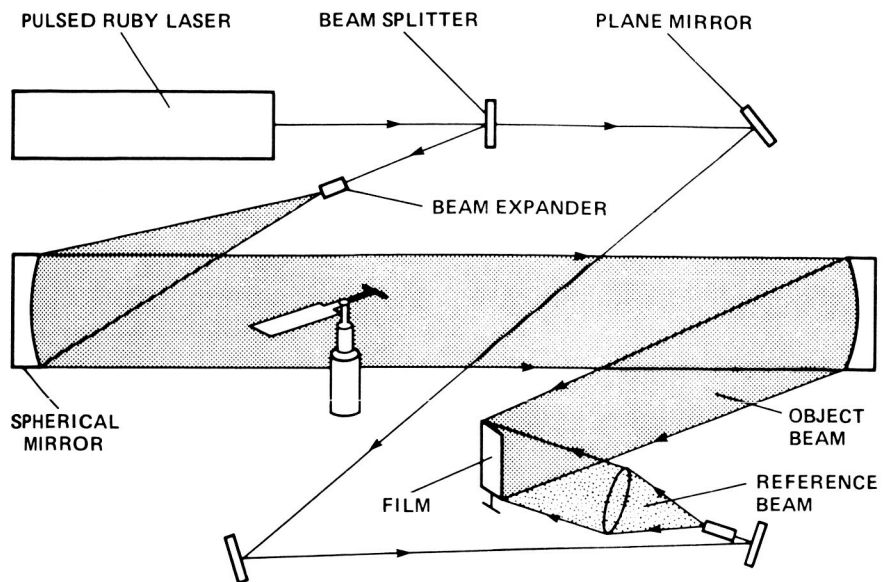
Fig. 5 Schematic drawing of the holographic recording system.
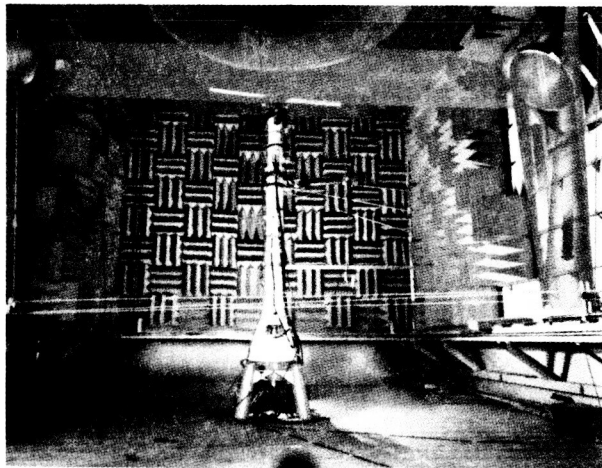
Fig. 6 Holographic setup at Anechoic Hover Chamber.
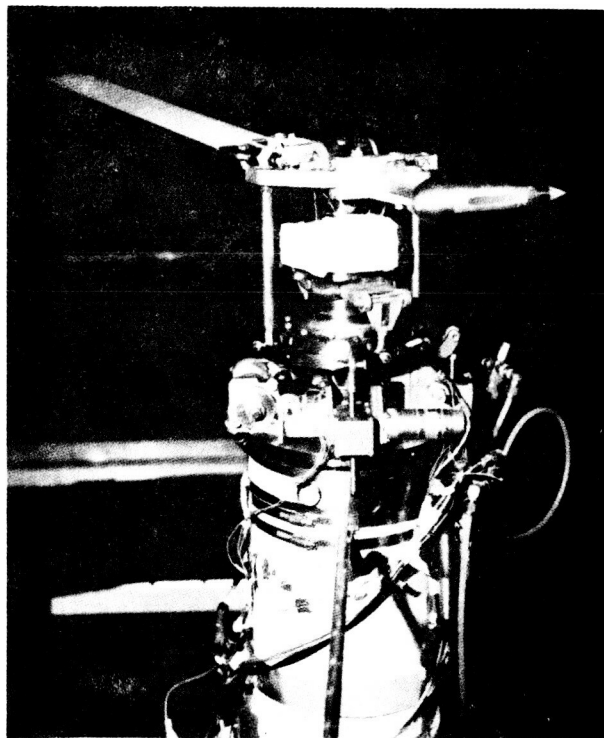
Fig. 7 One-blade rotor with a counterweight balance.

$\theta = 20°$
(a)

$\theta = 30°$
(b)

$\theta = 34°$
(c)

$\theta = 0°$

$\theta = 90°$
(d)

$\theta = 180°$

$\theta = 166°$
(e)

$\theta = 180°$
(f)

FILM

$\theta = 186°$
(g)
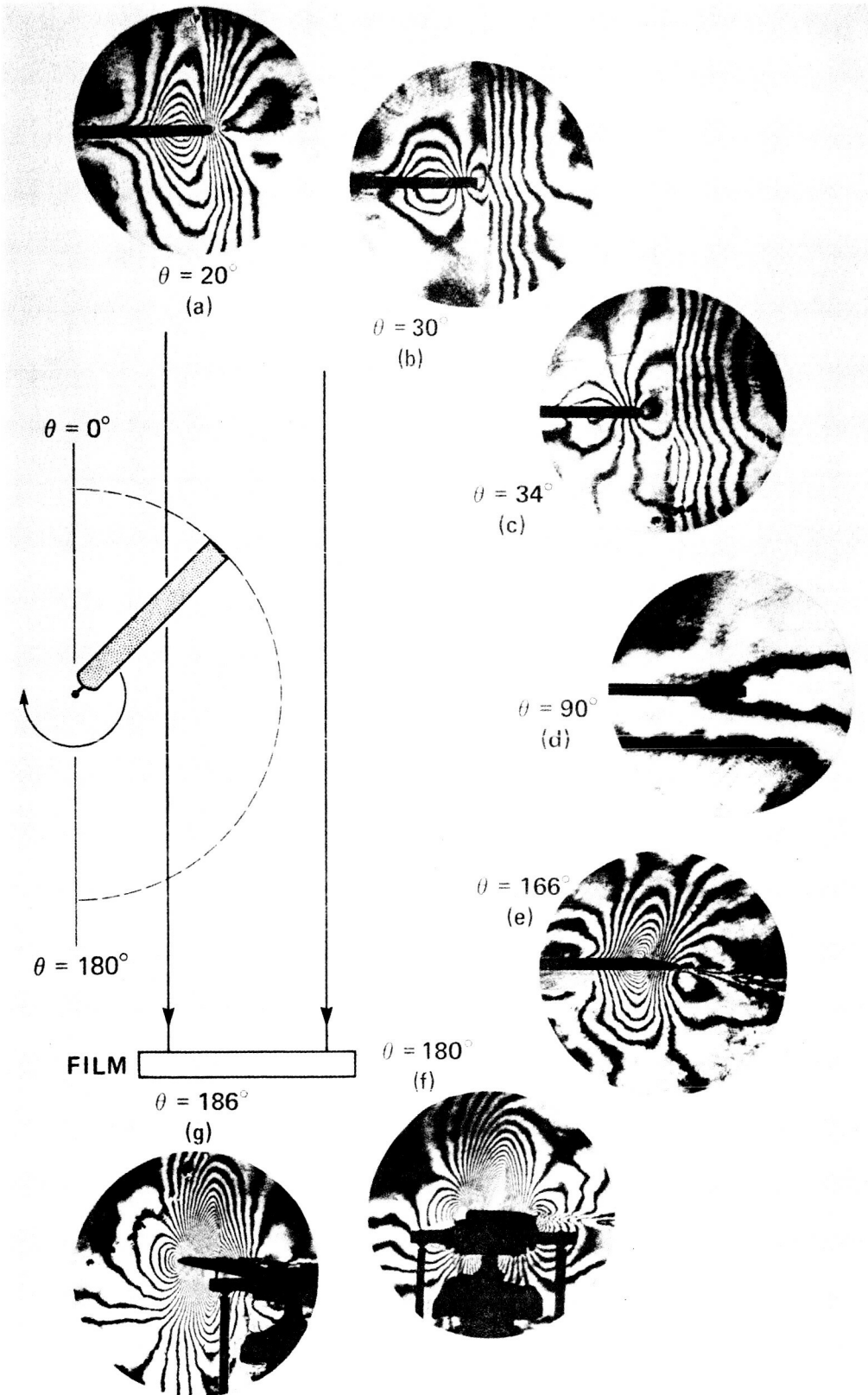
Fig. 8   Example interferograms recorded at various azimuthal angles.

159

(a)

(b)

(a)

(b)
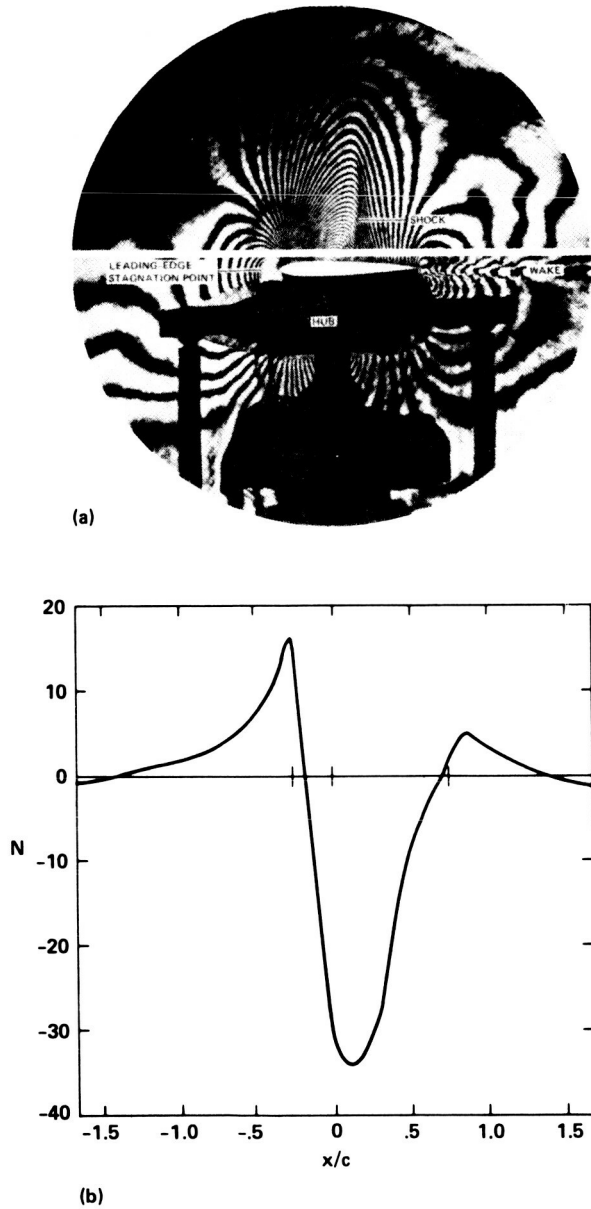
Fig. 9 Data extraction.   a) One-dimensional
interferogram evaluation is performed by scanning
each interferogram at a chosen height above the
blade surface; b) fringe-order numbers and coordi-
nates are recorded as input to the CAT code.
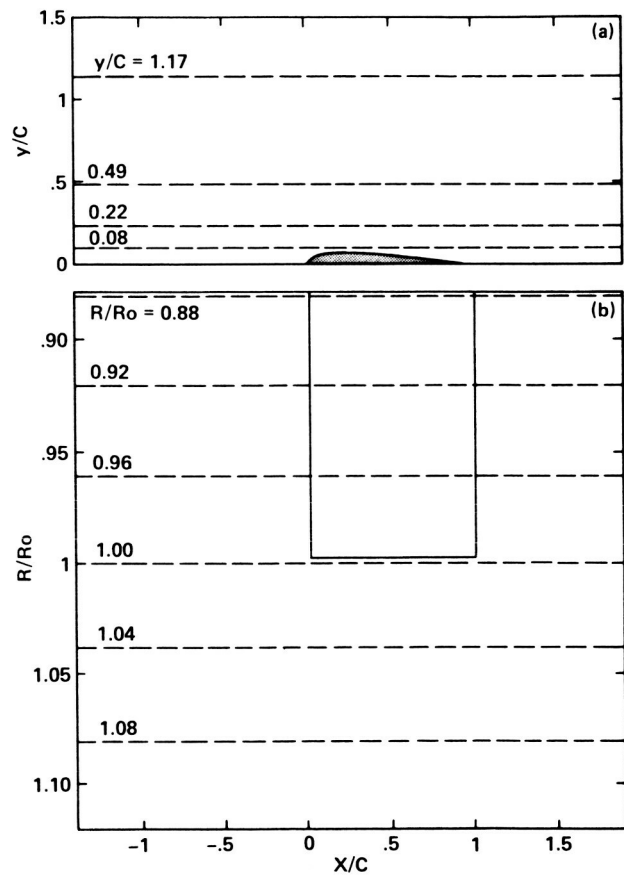
Fig. 10 Reconstructed flow-field geometry.
a) Location of four horizontal planes for velocity
contour maps and perspective views; b) location
of six radial stations for velocity distribution
plots.
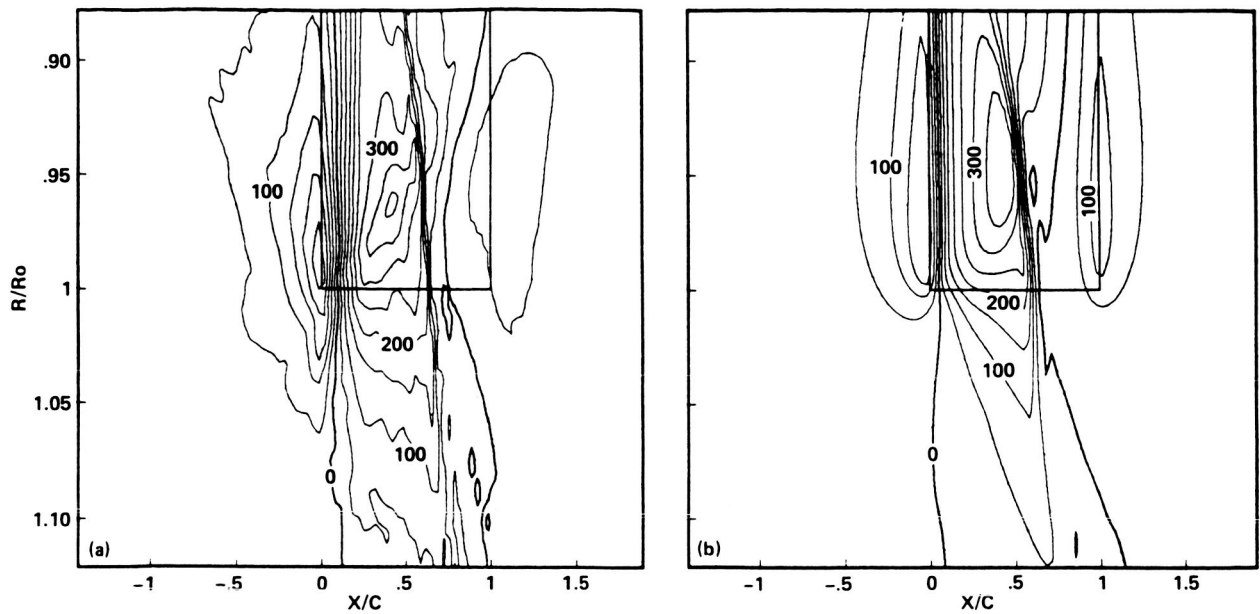
Fig. 11 Perturbation velocity contours in plan view for Y/C = 0.08 above blade centerline: contour interval = 50 ft/sec. a) Holography-CAT reconstruction; b) numerical code.
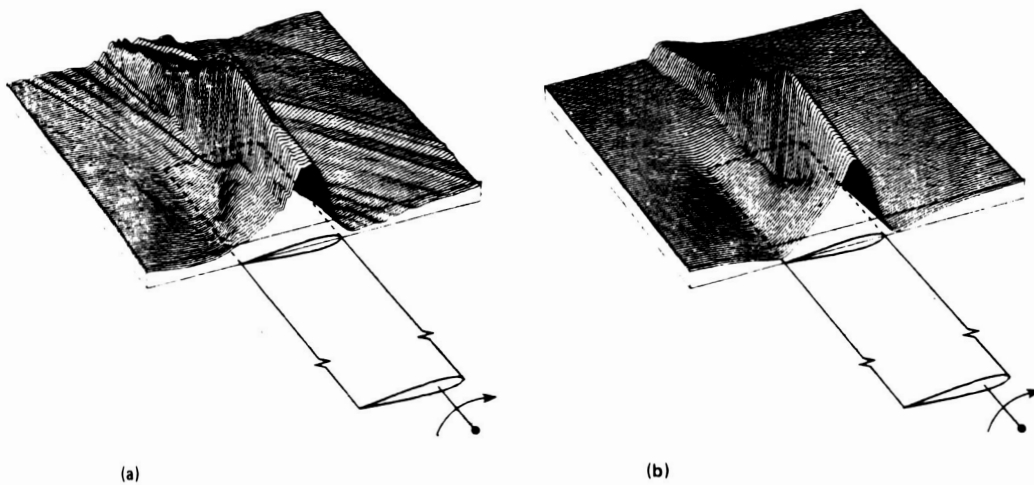

(a)   (b)
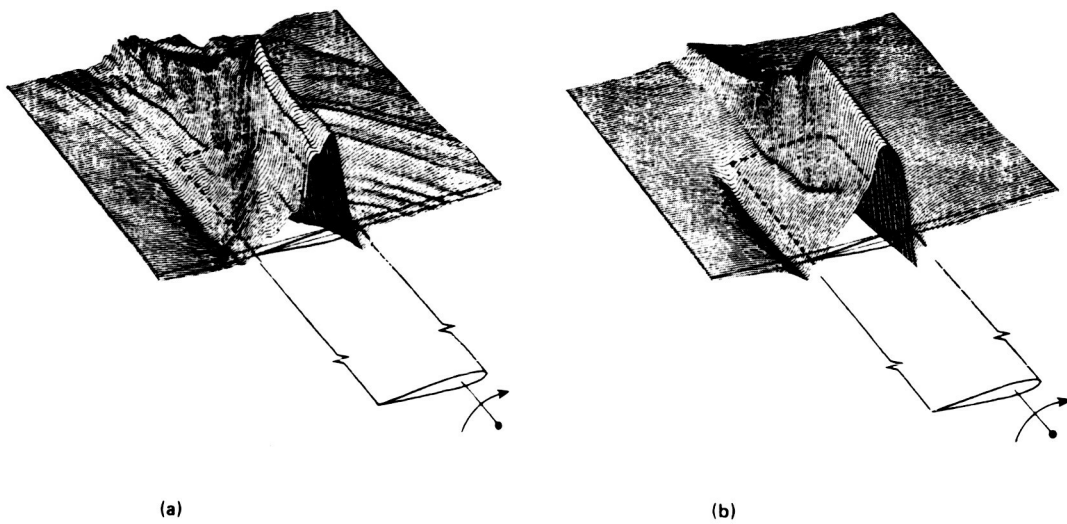
Fig. 12 Perturbation velocity values for Y/C = 0.08 above blade centerline. a) Holography-CAT reconstruction; b) numerical solution.
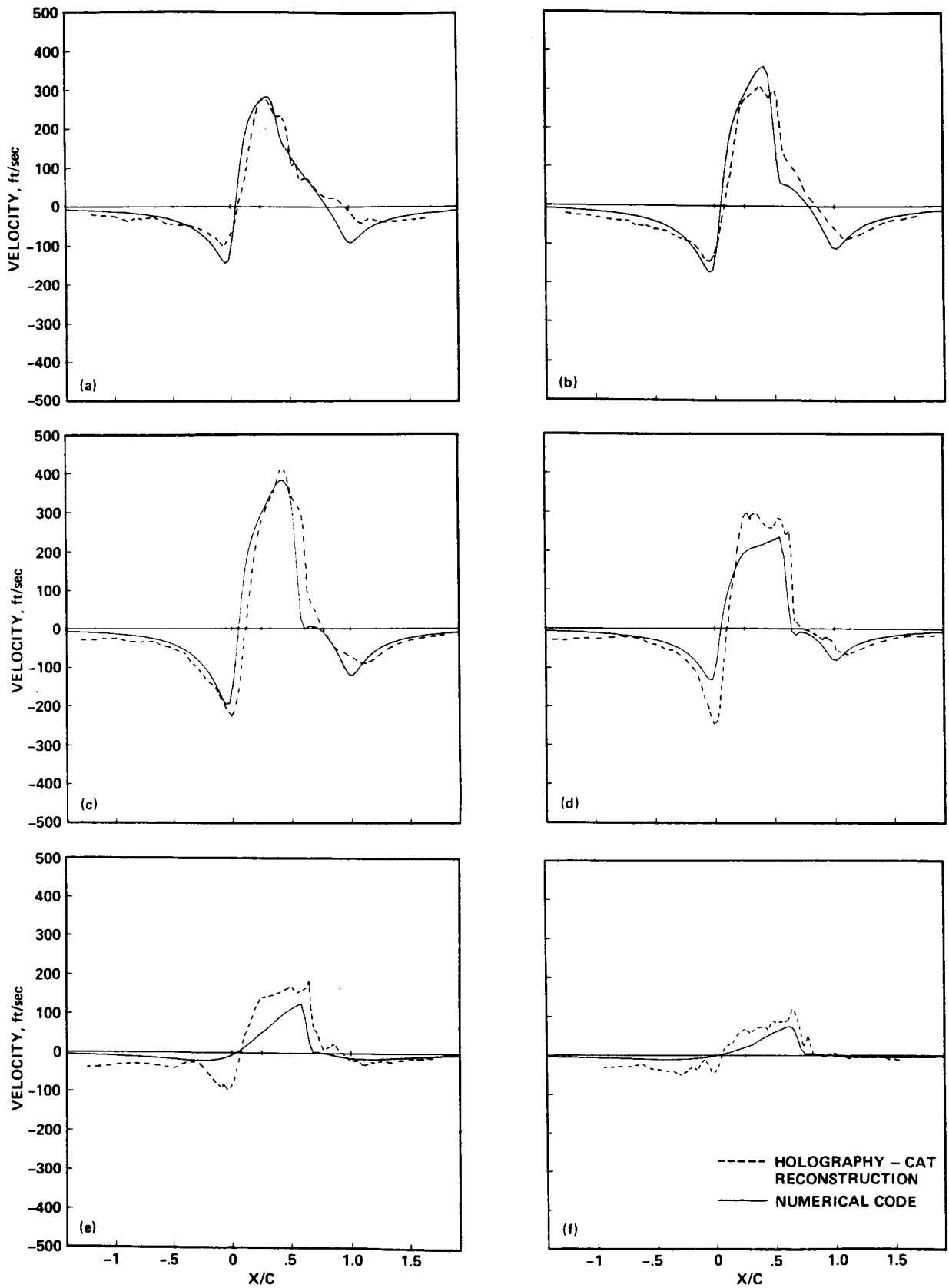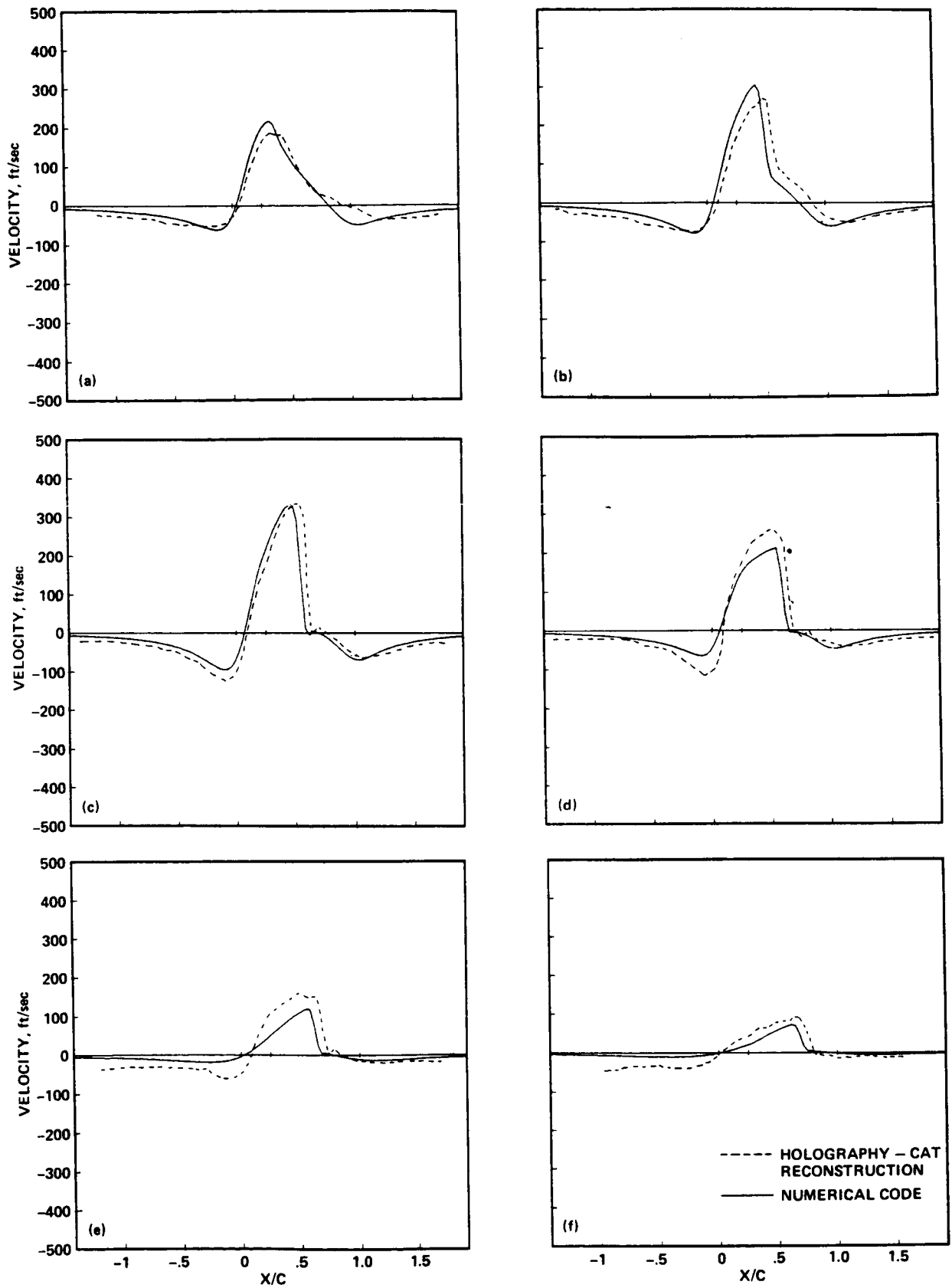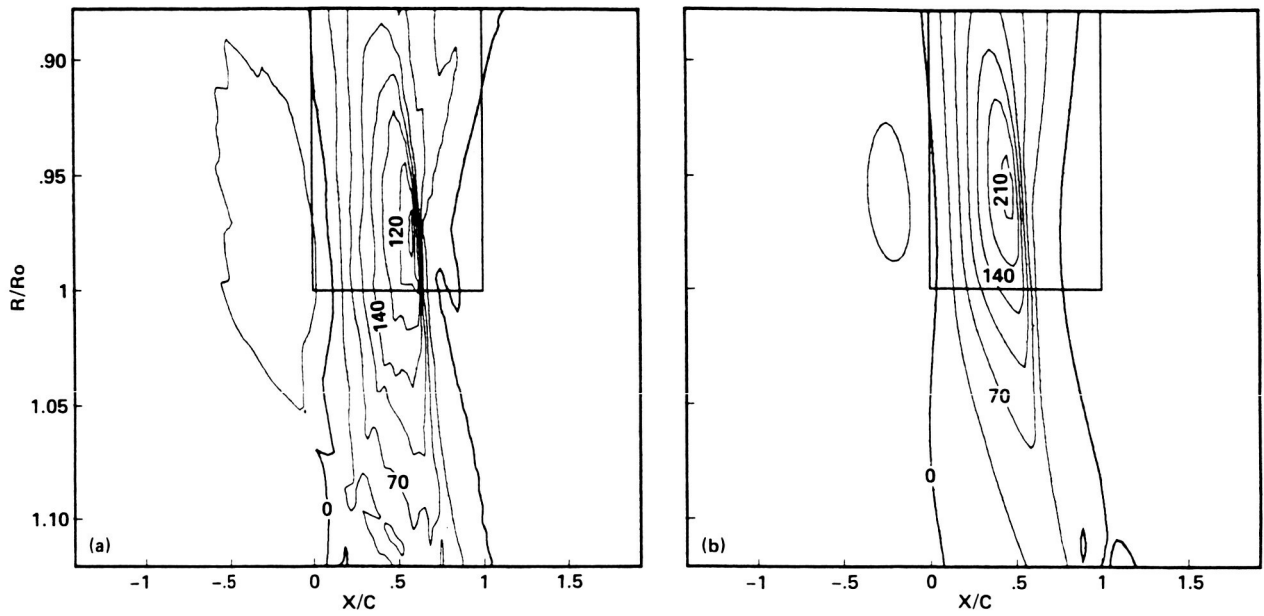
Fig. 13 Perturbation velocity distributions at six radial locations for Y/C = 0.08 above blade centerline. a) R/R_0 = 0.88; b) R/R_0 = 0.92; c) R/R_0 = 0.96; d) R/R_0 = 1.00; e) R/R_0 = 1.04; f) R/R_0 = 1.08.

Fig. 14 Schlieren photographs illustrating lambda shock on a NACA 0012 airfoil operating at a tip Mach number of 0.90 in forward flight. (From Ref. 25.)
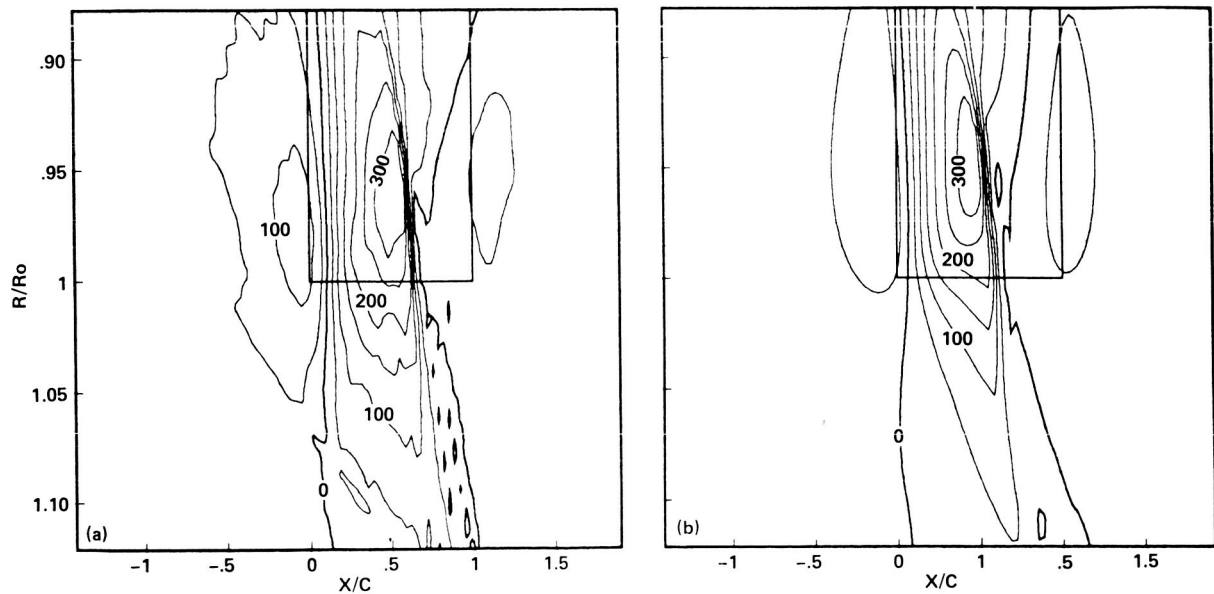
Fig. 15 Perturbation velocity contours in plan view for Y/C = 0.22 above blade centerline: contour interval = 50 ft/sec. a) Holography-CAT reconstruction; b) numerical code.
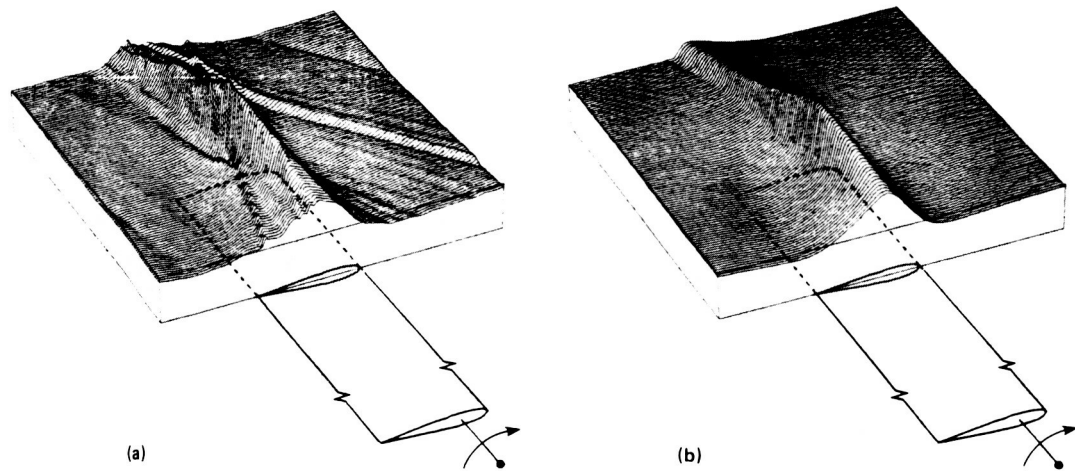
(a)

(b)

Fig. 16 Perturbation velocity values for Y/C = 0.22 above blade centerline. a) Holography–CAT
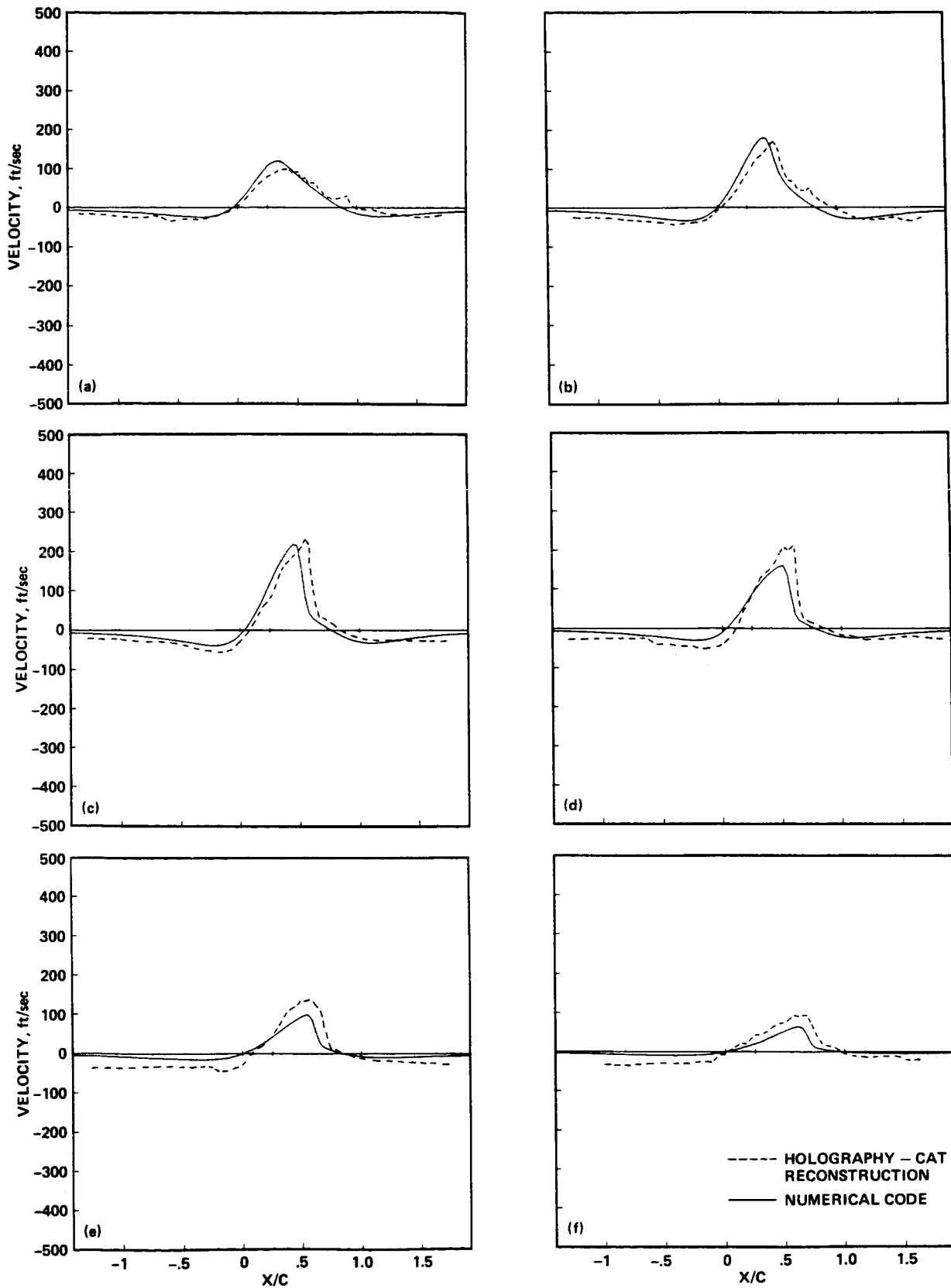reconstruction; b) numerical solution.

Fig. 17 Perturbation velocity distributions at six radial locations for Y/C = 0.22   above blade center-
line.   a) R/R_0= 0.88; b) R/R_0 = 0.92; c) R/R_0 = 0.96; d) R/R_0 = 1.00; e) R/R_0 = 1.04; f) R/R_0 = 1.08.
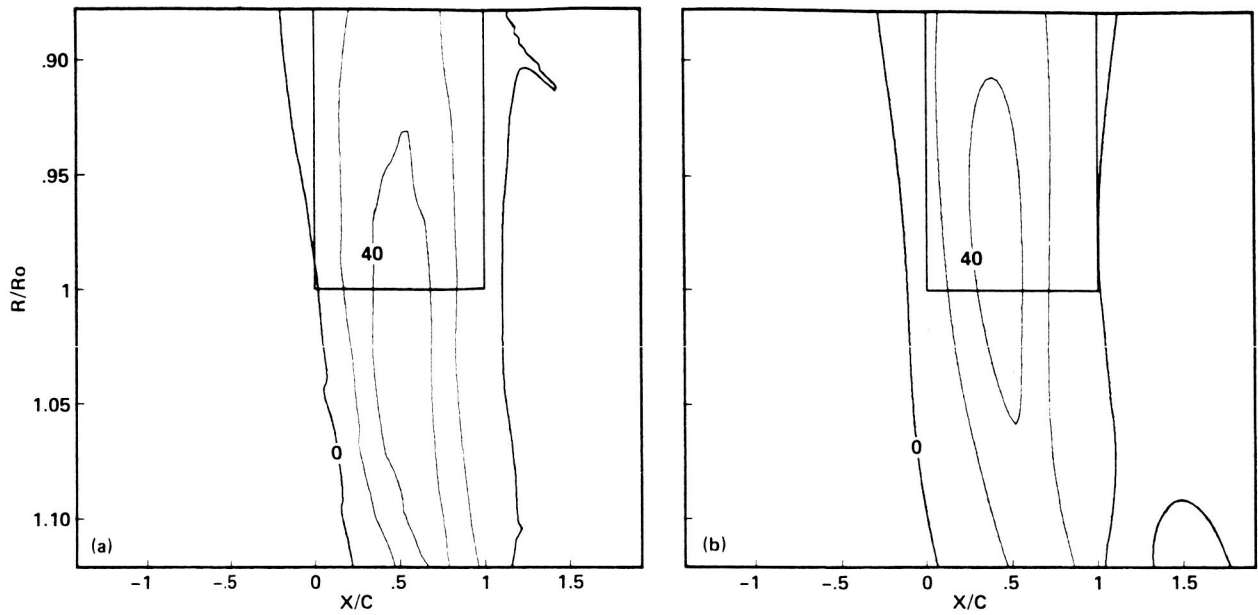
Fig. 18 Perturbation velocity contours in plan view for Y/C = 0.49 above blade centerline: contour interval = 35 ft/sec. a) Holography CAT-reconstruction; b) numerical code.

Fig. 19 Perturbation velocity values for Y/C = 0.49 above blade centerline. a) Holography-CAT reconstruction; b) numerical solution.

Fig. 20 Perturbation velocity distributions at six radial locations for Y/C = 0.49   above blade center-
line.   a) R/R_0 = 0.88; b) R/R_0 = 0.92; c) R/R_0 = 0.96; d) R/R_0 = 1.00; e) R/R_0 = 1.04; f) R/R_0 = 1.08.

Fig. 21 Perturbation velocity contours in plan view for Y/C = 1.17 above blade centerline: contour interval = 20 ft/sec. a) Holograph-CAT reconstruction; b) numerical code.
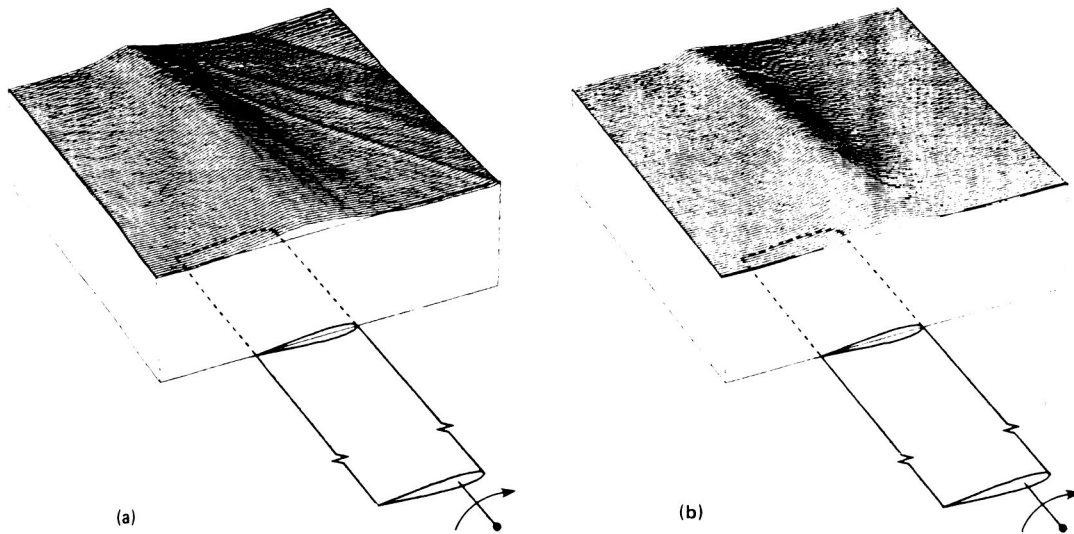

Fig. 22 Perturbation velocity values for Y/C = 1.17 above blade centerline. a) Holography-CAT reconstruction; b) numerical solution.
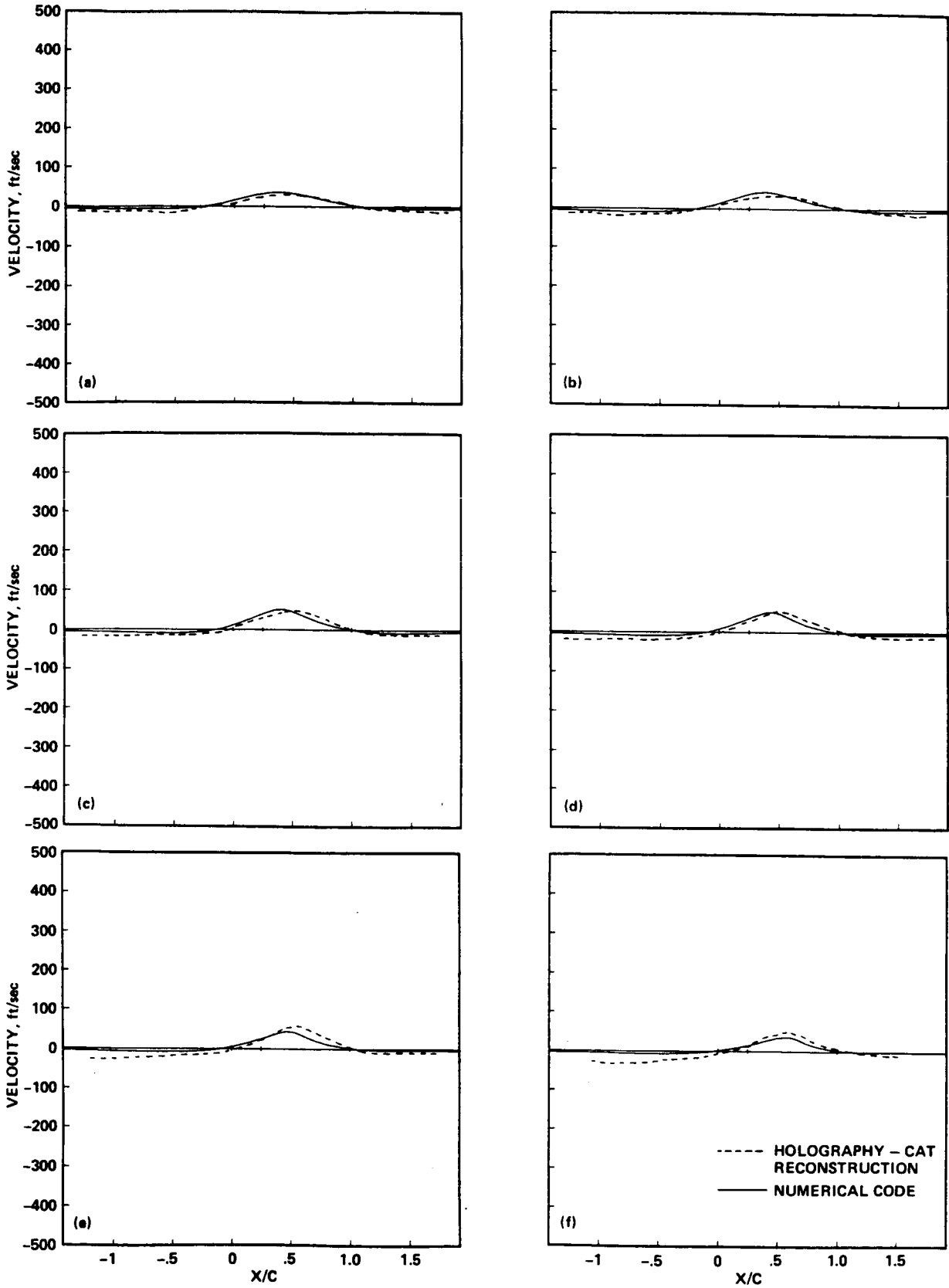
Fig. 23 Perturbation velocity distributions at six radial locations for Y/C = 1.17 above blade center-line. a) R/R₀ = 0.88; b) R/R₀ = 0.92; c) R/R₀ = 0.96; d) R/R₀ = 1.00; e) R/R₀ = 1.04; f) R/R₀ = 1.08.
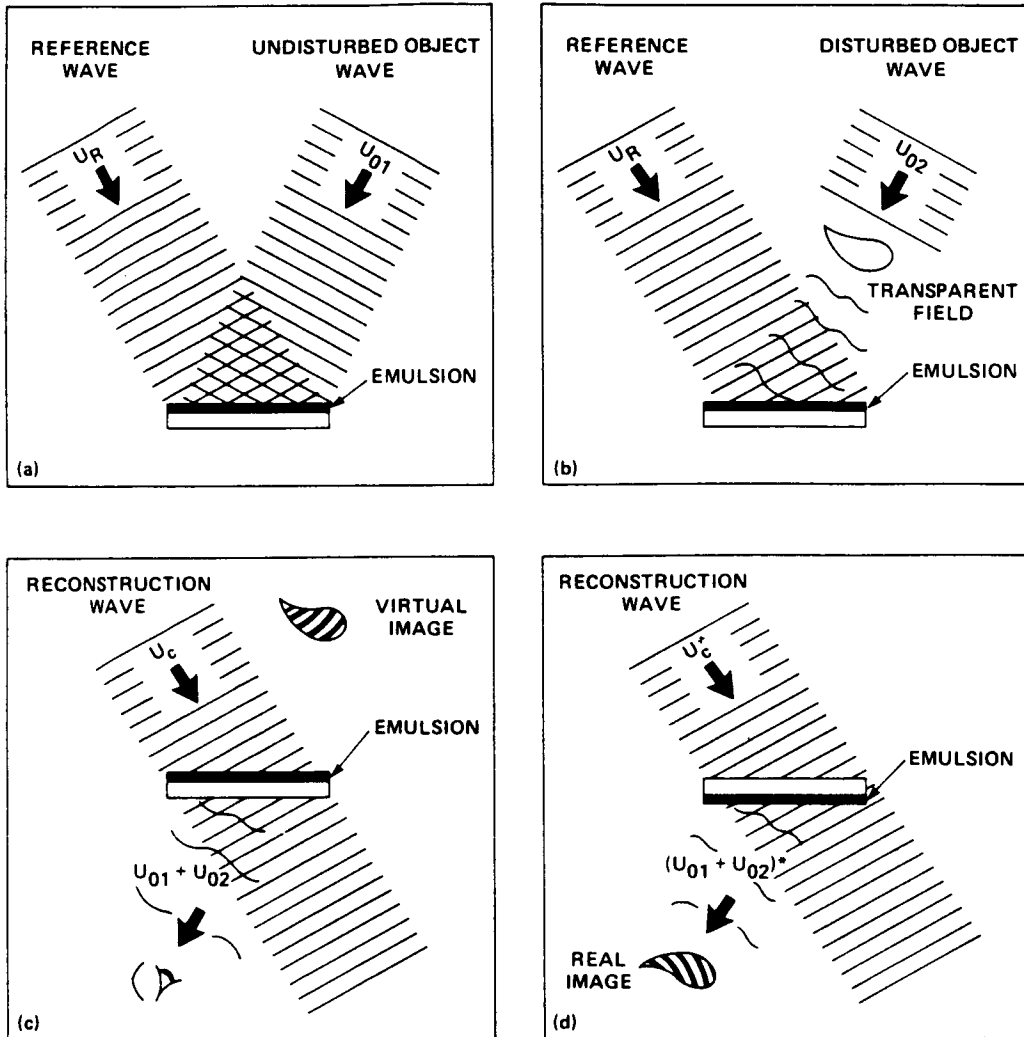
Fig. 24 Double-exposure holographic interferometry. a) First-exposure recording; b) second-exposure recording; c) reconstruction of the virtual image; d) reconstruction of the real image.